The Astrophysical Journal, 948:133 (12pp), 2023 May 10 https://doi.org/10.3847/1538-4357/acc584

Detection of Interstellar *E*-1-cyano-1,3-butadiene in GOTHAM Observations of TMC-1

Ilsa R. Cooke[1], Ci Xue[2], P. Bryan Changala[3], Hannah Toru Shay[2], Alex N. Byrne[2], Qi Yu Tang[1], Zachary T. P. Fried[2], Kin Long Kelvin Lee[2,4], Ryan A. Loomis[5], Thanja Lamberts[6,7], Anthony Remijan[5], Andrew M. Burkhardt[8], Eric Herbst[9,10], Michael C. McCarthy[3], and Brett A. McGuire[2,5]

[1] Department of Chemistry, University of British Columbia, 2036 Main Mall, Vancouver, BC, V6T 1Z1, Canada; icooke@chem.ubc.ca
[2] Department of Chemistry, Massachusetts Institute of Technology, Cambridge, MA 02139, USA; brettmc@mit.edu
[3] Center for Astrophysics | Harvard & Smithsonian, Cambridge, MA 02138, USA
[4] Accelerated Computing Systems and Graphics Group, Intel Corporation, 2111 25th NE Avenue, Hillsboro, OR 97124, USA
[5] National Radio Astronomy Observatory, Charlottesville, VA 22903, USA
[6] Leiden Institute of Chemistry, Gorlaeus Laboratories, Leiden University, P.O. Box 9502, 2300 RA Leiden, The Netherlands
[7] Leiden Observatory, Leiden University, P.O. Box 9513, 2300 RA Leiden, The Netherlands
[8] Department of Physics, Wellesley College, Wellesley, MA 02481, USA
[9] Department of Chemistry, University of Virginia, Charlottesville, VA 22904, USA
[10] Department of Astronomy, University of Virginia, Charlottesville, VA 22904, USA

Received 2022 December 28; revised 2023 March 15; accepted 2023 March 18; published 2023 May 17

Abstract

We report the detection of the lowest-energy conformer of *E*-1-cyano-1,3-butadiene (*E*-1-C_4H_5CN), a linear isomer of pyridine, using the fourth data reduction of the GBT Observations of TMC-1: Hunting for Aromatic Molecules (GOTHAM) deep spectral survey toward TMC-1 with the 100 m Green Bank Telescope. We perform velocity stacking and matched-filter analyses using Markov chain Monte Carlo simulations and find evidence for the presence of this molecule at the 5.1σ level. We derive a total column density of $3.8^{+1.0}_{-0.9} \times 10^{10}$ cm^{-2}, which is predominantly found toward two of the four velocity components we observe toward TMC-1. We use this molecule as a proxy for constraining the gas-phase abundance of the apolar hydrocarbon 1,3-butadiene. Based on the three-phase astrochemical modeling code NAUTILUS and an expanded chemical network, our model underestimates the abundance of cyano-1,3-butadiene by a factor of 19, with a peak column density of 2.34×10^{10} cm^{-2} for 1,3-butadiene. Compared to the modeling results obtained in previous GOTHAM analyses, the abundance of 1,3-butadiene is increased by about two orders of magnitude. Despite this increase, the modeled abundances of aromatic species do not appear to change and remain underestimated by one to four orders of magnitude. Meanwhile, the abundances of the five-membered ring molecules increase proportionally with 1,3-butadiene by two orders of magnitude. We discuss the implications for bottom-up formation routes to aromatic and polycyclic aromatic molecules.

Unified Astronomy Thesaurus concepts: Astrochemistry (75); Polycyclic aromatic hydrocarbons (1280); Chemical abundances (224); Dark interstellar clouds (352); Interstellar molecules (849)

1. Introduction

The dark prestellar cloud TMC-1, in the Taurus Molecular Cloud complex, has been extensively observed, revealing a rich molecular inventory, including carbon-chain neutral species, positive and negative ions, and nitrogen-bearing species (Gratier et al. 2016). More recently, the discovery of benzonitrile (*c*-C_6H_5CN) by McGuire et al. (2018) added the first aromatic ring to this inventory. Following this detection, a number of additional aromatic and unsaturated cyclic molecules have been detected using our GBT Observations of TMC-1: Hunting for Aromatic Molecules (GOTHAM) line survey (Burkhardt et al. 2021b; Lee et al. 2021b; McCarthy et al. 2021; McGuire et al. 2021) and the *Q*-band Ultrasensitive Inspection Journey to the Obscure TMC-1 Environment (QUIJOTE) survey of Cernicharo and colleagues (Cernicharo et al. 2021a, 2021b, 2021c, 2022).

In order to understand the formation of aromatic molecules and other cyclic species, gas-grain chemical models (e.g., NAUTILUS; Ruaud et al. 2016) combined with large reaction networks (e.g., Wakelam et al. 2015) have been used. These models, however, cannot currently reproduce the observed abundance of these aromatic molecules, which may be in part due to the lack of observational constraints on potential precursors (Burkhardt et al. 2021a). Small, unsaturated hydrocarbons are suggested to be involved in the bottom-up formation of aromatic molecules. However, many unsaturated and partially saturated hydrocarbons have not yet been detected in TMC-1 and thus are large unknowns for these models. As such, in order to determine the formation pathways of even the simplest aromatics, robust abundance measurements of potential precursor species must be obtained.

In laboratory experiments under single-collision conditions, Jones et al. (2011) showed that benzene (C_6H_6) can readily form via the neutral–neutral reaction between the ethynyl radical (C_2H) and 1,3-butadiene ($CH_2CHCHCH_2$):

$$CH_2CHCHCH_2 + C_2H \longrightarrow C_6H_6 + H. \quad (1)$$

Electronic structure calculations showed the reaction is barrierless and exoergic, forming C_6H_6 through a complex-forming reaction mechanism. The thermodynamically less stable hexa-1,3-dien-5-yne isomer ($HCCCHCHCHCH_2$) of benzene was found to be the dominant reaction product under

single-collision conditions, whereas the branching ratio to C_6H_6 was 30% ± 10%.

Lockyear et al. (2015) studied the products of this reaction under thermal conditions in a flow reactor using synchrotron photoionization mass spectrometry. The photoionization spectra indicated, in contrast to the observations of Jones et al. (2011), that the fulvene ($(CHCH)_2CCH_2$) isomer of benzene is the major reaction product, with a branching fraction of ∼60%. They did not detect C_6H_6 as a product at all and placed an upper limit on the branching fraction for the sum of the C_6H_6 and $HCCCHCHCHCH_2$ isomers of 45%. Lee & McCarthy (2019) likewise observed evidence for $(CHCH)_2CCH_2$ formation in a microwave discharge containing HC_3N (used as a C_2H precursor) and $CH_2CHCHCH_2$; C_6H_6 could not be constrained in their work since rotational spectroscopy was used as the detection method.

$CH_2CHCHCH_2$ is therefore a critical yet unconstrained precursor to aromatic and cyclic molecules in TMC-1. However, since the lowest-energy conformer of $CH_2CHCHCH_2$ does not possess a dipole moment, it is invisible to radio astronomy. Searching instead for an analog of that molecule which has been "tagged" with a polar functional group, such as the nitrile (or cyano) unit, –C ≡ N, yields a spectroscopically bright surrogate. Indeed, the first detections of a benzene-ring species with radio astronomy, and individual interstellar polycyclic aromatic hydrocarbon (PAH) molecules in general, were those of the nitrile derivatives of C_6H_6 and naphthalene ($C_{10}H_8$), namely benzonitrile (C_6H_5CN; McGuire et al. 2018) and cyanonapthalene (1- and 2-$C_{10}H_7CN$; McGuire et al. 2021), respectively. Laboratory and theoretical studies indicate that nitrile functionalization of unsaturated hydrocarbons occurs facilely via CN-addition and H-elimination processes across a double bond (Sims et al. 1993; Balucani et al. 2000). This makes the observation of CN-substituted surrogates a potentially broadly applicable tool for quantifying otherwise radio-dark symmetric hydrocarbons. Recent observations and astrochemical models, comparing the ratio of pure aromatic hydrocarbons to their CN-functionalized counterparts, support this proxy method (Sita et al. 2022).

The reaction of CN with $CH_2CHCHCH_2$ has been studied extensively both in the laboratory and computationally (Morales et al. 2011; Sun et al. 2014). Morales et al. (2011) used crossed molecular beams to investigate the reaction products under single-collision conditions and uniform supersonic flows to measure the reaction kinetics as a function of temperature. Their measurements demonstrated that at low temperatures the overall reaction is fast, close to the gas-kinetic limit, and that the 1-cyano-1,3-butadiene (1-C_4H_5CN) isomer is the dominant reaction product. They also suggested that possible minor fractions of the aromatic pyridine isomer (*c*-C_5H_5N) could form in this reaction, a heterocycle which has thus far eluded detection in the interstellar medium (ISM; Barnum et al. 2022). We were therefore motivated to search for 1-C_4H_5CN in TMC-1 as a chemical proxy for $CH_2CHCHCH_2$. Recently, Zdanovskaia et al. (2021) reported millimeter-wave rotational spectra of three isomers of cyano-butadiene: the s-*trans conformers of E*-1-cyano-1,3-butadiene and*Z*-1-cyano-1,3-butadiene, and the syn and *anti* conformers of 4-cyano-1,2-butadiene, and -4-cyano-1,2-butadiene, extending the centimeter-wave measurements of the *E*- and *Z*- stereoisomers reported by McCarthy et al. (2020). These new laboratory measurements, facilitated by the synthesis of these molecules (Kougias et al. 2020), provide the foundation for our astronomical search.

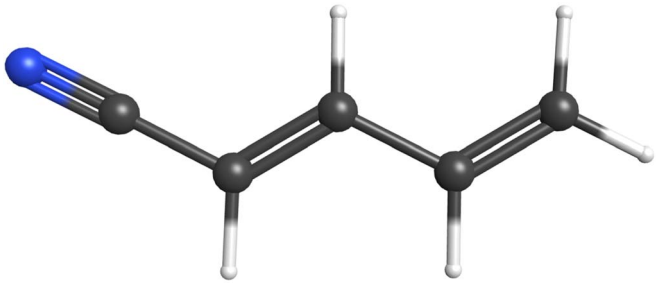

Figure 1. The chemical structure of s-*trans*-*E*-1-cyano-1,3-butadiene.

We therefore perform a dedicated astronomical search for cyano-butadiene isomers with the GOTHAM spectral survey. The observations are described in Section 2. Section 3.1 presents the observational analyses and the detection of s-*trans*-*E*-1-cyano-1,3-butadiene, which we hereafter refer to as *E*-1-C_4H_5CN for simplicity. The chemical structure of the s-*trans* conformer is shown in Figure 1. The observed results are used to constrain the new chemical network developed for 1-C_4H_5CN and its isomer *c*-C_5H_5N in Section 3.2. In Section 4, we discuss the implications of constraining the abundance of 1-C_4H_5CN and the future searches for *c*-C_5H_5N. Finally, we summarize our results in Section 5.

2. Observations

We performed a search toward TMC-1 using the fourth data reduction of the GOTHAM collaboration survey. GOTHAM is a large project performed with the 100 m Robert C. Byrd Green Bank Telescope (GBT). The GOTHAM program is a dedicated spectral-line observing program of TMC-1 covering almost 30 GHz of bandwidth at high sensitivity and spectral resolution. Details of the source, observations, and data-reduction methods can be found in McGuire et al. (2020) and McGuire et al. (2021). Briefly, the spectra in these data cover the entirety of the X-, K-, and Ka-receiver bands with nearly continuous coverage from 7.9 to 11.6 GHz, 12.7 to 15.6 GHz, and 18.0 to 36.4 GHz (24.9 GHz of total bandwidth). Observations were performed with the project codes GBT17A-164, GBT17A-434, GBT18A-333, GBT18B-007, GBT19B-047, AGBT20A-516, AGBT21A-414, and AGBT21B-210.

The first, second, and third data reductions of GOTHAM (hereafter referred to as DR1, DR2, and DR3, respectively) comprise observations obtained between 2018 February–2019 May (DR1), 2020 June (DR2), and 2021 April (DR3; McGuire et al. 2020, 2021). The GOTHAM observations used here are the fourth data reduction (DR4), which comprises observations made through 2022 May. DR4 extends the frequency coverage from 7.906 to 36.411 GHz (24.9 GHz total observed bandwidth), with a few gaps, and improved the sensitivity in some frequency coverage already covered by DR2. A full description of DR4 can be found in Sita et al. (2022).

The pointing was centered on the TMC-1 cyanopolyyne peak at (J2000) $\alpha = 04^h41^m42\overset{s}{.}50 \delta = +25\ °41'26\overset{''}{.}8$. The spectra were obtained through position switching to an emission-free position 1° away. Pointing and focusing were refined every 1–2 hr, primarily on the calibrator J0530+1331. Flux calibration was performed with an internal noise diode and Karl G. Jansky Very Large Array observations of the same calibrator used for pointing, resulting in a flux uncertainty of

∼20% (McGuire et al. 2020; Sita et al. 2022). All data were taken with a uniform frequency resolution of 1.4 kHz (0.05–0.01 km s^{-1} in velocity). An rms noise of ∼2–20 mK was achieved across most of the observed frequency range, with the rms gradually increasing toward higher frequencies due to less total integration time at those settings.

3. Analysis and Results

3.1. Observational Analyses and Results

As of GOTHAM DR4, no individual transitions of the cyano-butadiene isomers were bright enough for identification. In the absence of strong individual lines, we used the spectral stacking and matched-filtering procedure detailed in Loomis et al. (2021) to determine the statistical evidence for the presence of this molecule. In summary, a small spectral window is extracted for each of the top 5% strongest predicted transitions, provided that there is no interloping emission ($>5\sigma$) present in the spectrum. Fiducial stacks for *Z*-1-cyano-1,3-butadiene did not reveal any signal of significance, whereas signal was observed for the *E*-isomer. In this case, a total of 434 rotationally resolved hyperfine transitions of 1-C_4H_5CN met these criteria with no interloping transitions detected. The windows were subsequently combined in velocity space, each weighted by the observational rms and the predicted flux.

We additionally carry out a forward-modeling procedure using `molsim` (Lee et al. 2021a) that simulates the molecular emission with a set of model parameters following the conventions of Turner (1991) for a single excitation temperature and accounting for the effect of optical depth. The parameters include the source size (SS), used for estimating beam dilution effects, radial velocity ($v_{\rm lsr}$), column density (N_T), excitation temperature ($T_{\rm ex}$), and the line width (ΔV). More details of our modeling approach can be found in Loomis et al. (2021).

Prior high-resolution observations of TMC-1 from both GOTHAM (Xue et al. 2020) and others (Dobashi et al. 2018, 2019) have found that most emission seen at centimeter wavelengths can be separated into contributions from four distinct velocity components within the larger structure, at approximately 5.4, 5.6, 5.8, and 6.0 km s^{-1} (Loomis et al. 2021). In our model these are assigned to independent sets of SS, $v_{\rm lsr}$, and N_T, while a uniform $T_{\rm ex}$ and ΔV are adopted, resulting in a total of 14 modeling parameters. To properly account for uncertainty and covariance between model parameters, we use affine-invariant Markov chain Monte Carlo (MCMC) sampling as implemented in `emcee`, estimating the likelihood for each given set of model parameters. As with previous work on aromatic and cyclic species (Lee et al. 2021b; McCarthy et al. 2021; McGuire et al. 2021), our choice of prior was on the basis of chemical similarity; the posterior for HC_9N was used as the prior distribution for the 1-C_4H_5CN MCMC modeling.

Following convergence of the sampling, the resulting posterior was analyzed using the `arviz` suite of routines. To assess the robustness of the detection, the simulated spectrum from the posterior mean is velocity stacked and cross-correlated with the observational velocity stack in a matched-filter analysis: the peak impulse response (σ) corresponds to the statistical significance. As with previous GOTHAM analyses, we adopt a 5σ threshold to classify a firm detection (Loomis et al. 2021).

Table 1
Summary Statistics of the Marginalized *E*-1-C_4H_5CN Posterior

$v_{\rm lsr}$ (km s^{-1})	Size ($''$)	N_T (10^{10}cm^{-2})	$T_{\rm ex}$ (K)	ΔV (km s^{-1})
$5.581^{+0.020}_{-0.022}$	258^{+165}_{-171}	$2.67^{+0.65}_{-0.57}$	$6.97^{+0.48}_{-0.48}$	$0.133^{+0.021}_{-0.020}$
$5.787^{+0.024}_{-0.032}$	267^{+158}_{-162}	$1.01^{+0.68}_{-0.71}$		
$5.901^{+0.045}_{-0.045}$	263^{+158}_{-162}	$0.08^{+0.34}_{-0.06}$		
$6.042^{+0.045}_{-0.043}$	250^{+169}_{-166}	$0.06^{+0.20}_{-0.04}$		
N_T (Total): $3.83^{+1.00}_{-0.91} \times 10^{10}$ cm^{-2}				

Notes. The quoted uncertainties correspond to the 16th and 84th percentiles (1σ for a Gaussian distribution). The total column density is derived from combining the column densities of each component in quadrature.

The resulting parameters from the MCMC inference to *E*-1-C_4H_5CN emission in the DR4 observational data are shown in Table 1; a corner plot, which provides a more holistic, visual depiction of the explored parameter space, is shown in Figure A1. In some cases, especially for less abundant species where there is not a clear detection in one or more of the velocity components, we find that a three-component model performs better (McGuire et al. 2020). The majority of the *E*-1-C_4H_5CN column density is detected in two velocity components, so we also ran MCMC inference assuming only two velocity components, the results of which can be seen in Figure A2, along with the resulting stacked spectrum and matched-filter response (Figure A3). We find both models result in similar total column densities.

The total column density derived from the DR4 data, assuming a four-velocity-component model, is $3.83^{+1.00}_{-0.91} \times 10^{10}$ cm^{-2}. We find a total column density of $3.94^{+0.87}_{-0.79} \times 10^{10}$ cm^{-2} when using two velocity components in our MCMC analysis. The radial velocities, modeled source sizes, excitation temperature, and line width are consistent with similar molecules (that are optically thin) detected in TMC-1. Using these posterior parameters, we generated a spectral stack and performed a matched-filtering analysis as described above. The results are shown in Figure 2. The evidence for a detection of *E*-1-C_4H_5CN in our data, as observed in the peak impulse response of the matched filter, is 5.1σ.

3.2. Astrochemical Modeling

To study the formation of 1-C_4H_5CN and related species, we adapted the three-phase chemical network model `NAUTILUS` v1.1 code (Ruaud et al. 2016). Originally based on the KIDA network, previous GOTHAM analyses expanded the reaction network to include numerous aromatic and carbon-chain species detected using GOTHAM data. In all these works the model (hereafter referred to as the GOTHAM DR1 model) was able to reproduce the observed abundances of the new carbon-chain molecules with reasonable accuracy (typically within a factor of <2.5; McGuire et al. 2020; Xue et al. 2020; Loomis et al. 2021; Shingledecker et al. 2021). The abundances of cyclic molecules, however, have been systematically underproduced in each iteration of the model (Burkhardt et al. 2021a; McCarthy et al. 2021; McGuire et al. 2021).

For this work, we introduced two new species into the chemical network: 1-C_4H_5CN and *c*-C_5H_5N. In our models, we do not distinguish between isomers of 1-C_4H_5CN, thus 1-C_4H_5CN refers to the total abundance of the acyclic

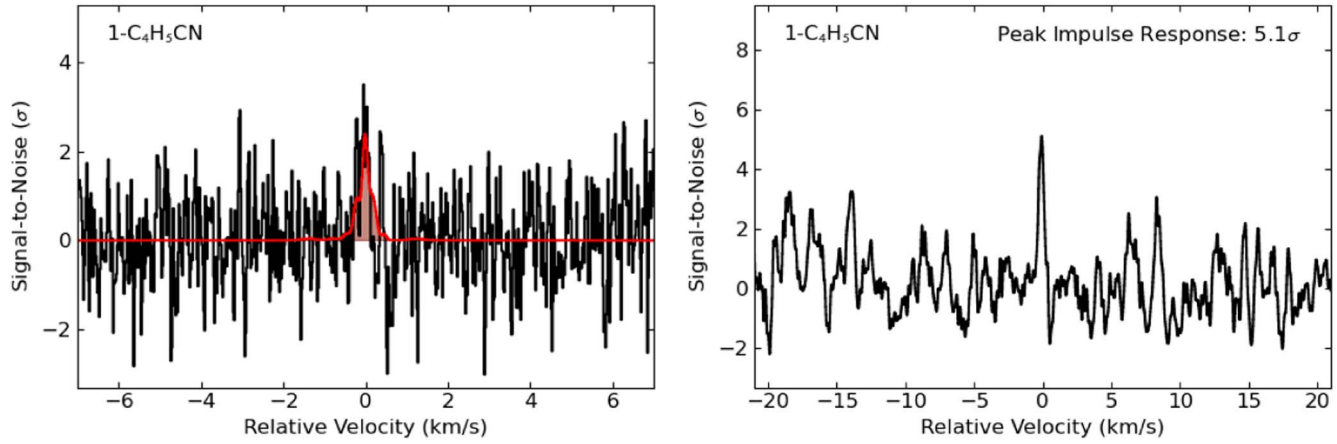

Figure 2. Velocity-stacked and matched-filter spectra of *E*-1-C_4H_5CN. The intensity scales are the signal-to-noise ratios (S/Ns) of the response functions when centered at a given velocity. The "zero" velocity corresponds to the channel with the highest intensity to account for blended spectroscopic transitions and variations in velocity component source sizes. Left: the stacked spectra from the GOTHAM DR4 data are displayed in black, overlaid with the expected line profile in red from our MCMC fit to the data. The S/N is on a per-channel basis. Right: matched-filter response obtained from cross-correlating the simulated and observed velocity stacks in the left panel; value annotated corresponds to the peak impulse response of the matched filter.

1-cyano-butadiene isomers. The production and destruction routes involving these molecules are summarized in Appendix B with the corresponding rate coefficients at 10 K. Low-temperature formation routes to 1-C_4H_5CN and *c*-C_5H_5N are not well known. One potential formation route is via dissociative recombination reactions between N-bearing hydrocarbon ions and electrons, which have been shown to dominate the formation of many carbon-chain molecules in cold environments. However, the formation of the precursor ions, such as $C_5H_6N^+$, is not well understood. Alternatively, laboratory studies have shown that CN radicals react efficiently with hydrocarbons to form the CN-substituted nitriles under low-temperature conditions (Sims et al. 1993; Cooke et al. 2020), as has been proposed for many CN-substituted hydrocarbons discovered in TMC-1. In this study, we assume the barrierless neutral–neutral reaction of $CH_2CHCHCH_2$ and the CN radical to be the only formation path for the two new species, i.e.,

$$\begin{aligned} CH_2CHCHCH_2 + CN &\longrightarrow 1\text{-}C_4H_5CN + H\,(99\%) \\ &\longrightarrow c\text{-}C_5H_5N + H\,1\,\%. \end{aligned}$$

Morales et al. (2011) measured the total rate coefficient from room temperature down to 23 K, and gave an expression for its temperature dependence as a modified Arrhenius expression:

$$k(T) = (4.8 \pm 0.1) \times 10^{-10} e^{\frac{-77 \pm 10}{8.31 \times T}}\ \mathrm{cm^3\,s^{-1}}, \qquad (2)$$

where T is the gas temperature in Kelvin. Experimental and computational studies further confirmed that the dominant product is 1-C_4H_5CN, with a possible minor amount (<1%) of *c*-C_5H_5N and an absence of 2-cyano-1,3-butadiene (Sun et al. 2014; Parker et al. 2015). As such, we assumed the branching fraction leading to 1-C_4H_5CN to be 99%. Other potential routes to *c*-C_5H_5N are discussed in Section 4.3.

The destruction of 1-C_4H_5CN and *c*-C_5H_5N were assumed to be analogous to that of cyanopolyynes under TMC-1 conditions (Woon & Herbst 2009). The most prevalent destruction pathways in the model are reactions with abundant cations (Appendix B). The reaction-rate coefficients of the related ion–molecule reactions were estimated with capture-rate theory (Woon & Herbst 2009) and Equation (1) from Xue et al. (2020). The dipole moment (μ) and average dipole polarizability (α) are $\mu = 4.814$ D and $\alpha = 11.178$ Å^3 for 1-C_4H_5CN (Zdanovskaia et al. 2021), and $\mu = 2.190$ D (Nelson et al. 1967) and $\alpha = 9.493$ Å^3 (Gray et al. 1984) for *c*-C_5H_5N.

For this study, the physical conditions of the model are assumed to be consistent with the previous modeling work of TMC-1 as part of the GOTHAM survey, originally constrained by Hincelin et al. (2011), with a gas and grain temperature of $T_{\rm gas} = T_{\rm grain} = 10$ K, a gas density of $n_{\rm H} = 2 \times 10^4\ \mathrm{cm^{-3}}$, a visual extinction of $A_{\rm v} = 10$, and a cosmic-ray ionization rate of $\zeta_{\rm CR} = 1.3 \times 10^{-17}\ \mathrm{s^{-1}}$. We adopted the initial elemental abundances described in Hincelin et al. (2011) with the exception of atomic oxygen. Through fitting the peak abundances of the cyanopolyyne family to the observed column densities, we previously determined that an O element abundance of 1.55×10^{-4}(/H), corresponding to a C/O ratio of 1.1, best reproduces our observations (Loomis et al. 2021). The resulting molecular abundances, with respect to an assumed $N_{\rm T,\,(H_2)} = 1 \times 10^{22}\mathrm{cm^{-2}}$ (Gratier et al. 2016), were converted to column densities and compared with the observed values. This $N_{\rm T,\,(H_2)}$ value is consistent with the H_2 column density map of TMC-1 derived from the dust continuum emission observed by Herschel (Smith et al. 2023).

In Figure 3, we present the results of the chemical modeling of 1-C_4H_5CN, *c*-C_5H_5N, and their precursor $CH_2CHCHCH_2$. The model at an age of $\sim 3.7 \times 10^5$ yr has a peak abundance of 2.28×10^{-13}(/H_2) for 1-C_4H_5CN, $5.9^{+1.4}_{-1.6}$% of the observed abundance. In addition, the model predicted an abundance of 4.8×10^{-15}(/H_2) for *c*-C_5H_5N and 2.34×10^{-12}(/H_2) for $CH_2CHCHCH_2$. Although the current model underpredicts the observed column density of 1-C_4H_5CN, the updates we have made here to the reaction network of the related species show substantial progress in bringing the models into alignment with observations. In this case, the modeled abundance of $CH_2CHCHCH_2$ (blue solid trace) is increased by about two orders of magnitude compared to the results obtained with the GOTHAM DR1 model (blue dashed–dotted trace).

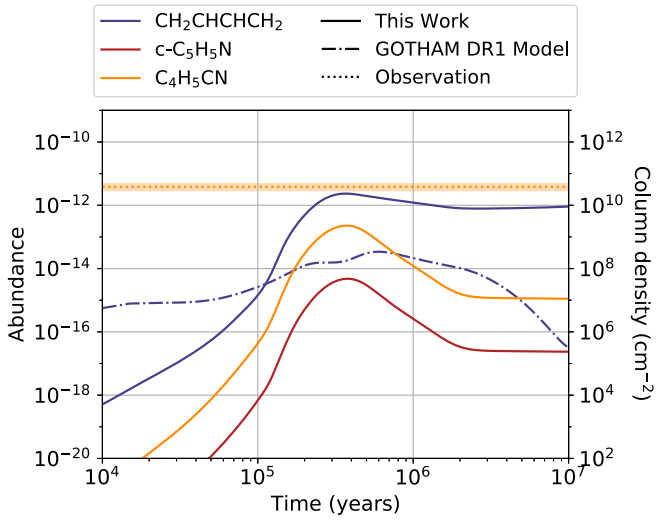

Figure 3. Models of $CH_2CHCHCH_2$ (blue), 1-C_4H_5CN (orange), and *c*-C_5H_5N (red) under TMC-1 conditions. Model results obtained with the modified network presented in this work are shown with solid traces, whereas those obtained with GOTHAM DR1 are shown with a dashed–dotted trace. The observed abundance of 1-C_4H_5CN is indicated by the dotted dark purple line along with the uncertainties.

4. Discussion

4.1. Butadiene

The lack of a permanent dipole moment makes it impossible to detect $CH_2CHCHCH_2$ through its rotational spectra. In contrast, its cyano derivative, 1-C_4H_5CN, potentially provides an indirect constraint on the gas-phase abundance of $CH_2CHCHCH_2$ based on the X-CN:X-H ratio. While the absolute abundance of 1-C_4H_5CN predicted by our model still falls well below the observed value, we have recently shown that our models are remarkably good at reproducing the observed X-CN:X-H ratio of CN-substituted:hydrocarbon species. This was recently demonstrated by Sita et al. (2022) through the direct observation of the hydrocarbon PAH indene (C_9H_8) and its CN-substituted counterpart, 2-cyanoindene (C_9H_7CN). A $C_9H_8/2$-C_9H_7CN ratio of 43 was observed, which is fairly consistent with the model's predicted ratio. Comparing the model-predicted ratios against their observed ratios, they found the model was accurate to within a factor of ∼2–5 for a range of X-CN:X-H pairs, providing evidence that cyano-PAHs may be considered robust observational proxies for their hydrocarbon counterparts.

The dominant gas-phase pathways leading to the formation of $CH_2CHCHCH_2$ at low temperature include the reaction of the methylidyne radical (CH) with propene (CH_3CHCH_2):

$$CH_3CHCH_2 + CH \longrightarrow CH_2CHCHCH_2 + H, \quad (3)$$

and *n*-propyl radicals ($CH_2CH_2CH_3$) reacting with atomic carbon:

$$CH_2CH_2CH_3 + C \longrightarrow CH_2CHCHCH_2 + H. \quad (4)$$

The total rate constant of the reactions between CH_3CHCH_2 and CH was measured to be $3.86–4.58 \times 10^{-10}$ cm^3 $molecule^{-1}$ s^{-1} over a temperature range of 70–170 K (Daugey et al. 2005) and $4.2 \pm 0.8 \times 10^{-10}$ cm^3 $molecule^{-1}$ s^{-1} at 298 K (Loison & Bergeat 2009). While Loison & Bergeat (2009) reported a branching ratio of (78 ± 10)% for the H atom production channel, another recent experiment reported a branching ratio of (63 ± 13)% for the $CH_2CHCHCH_2$ channel at 298 K (Trevitt et al. 2013). Considering that Trevitt et al. (2013) did not constrain the total rate constant, we use a rate constant of 3.3×10^{-10} cm^3 $molecule^{-1}$ s^{-1} for Reaction (3) in our models to be consistent, following the suggestion of Loison & Bergeat (2009) and Loison et al. (2017). Additional measurements of the overall rate coefficient for this reaction down to ∼10 K would be valuable.

Unlike in the gas phase, it seems unlikely that Reaction (3) would take place on the grain surface. Based on theoretical calculations, the potential energy surfaces for Reaction (3) proposed by Loison & Bergeat (2009) depict that the $CH_2CHCHCH_2$ + H and allene (H_2CCCH_2) + methyl radical (CH_3) channels are the most energetically stabilized. However, the calculations presented in Loison & Bergeat (2009) do not take any surface effect into account. Although the surface effect might not affect the reaction barrier heights so much, we expect it impacts the way the reactants sit on the surface and therefore the possible orientations for reactivity. Furthermore, while gaseous intermediates can cross a potential energy surface if it is overall exothermic, any intermediate in the solid state is likely to dissipate its energy fairly quickly. In this way, the C_4H_7 intermediates can stabilize, and an isomer of the C_4H_7 complex becomes the product of this reaction on grains. This suggests that Reaction (3) can efficiently produce $CH_2CHCHCH_2$ in the gas phase but may not do so on the grain surface, although there might be other surface pathways.

Carbon atoms have been proposed to react with hydrocarbons without any entrance barriers in interstellar environments (e.g., Kaiser et al. 1997; Chin et al. 2013). Based on capture-rate theory and the isomeric Reaction (3), Loison et al. (2017) suggested Reaction (4) with a rate constant of 1.6×10^{-10} cm^3 $molecule^{-1}$ s^{-1}. Along with Reaction (4), we also incorporated the gas-phase and grain reactions of the relevant three-carbon hydrocarbons, namely propyne (CH_3CCH), propenyl radical ($CHCHCH_3$), propene (CH_3CHCH_2), *n*-propyl radical ($CH_3CH_2CH_2$), and propane ($CH_3CH_2CH_3$), listed in Hickson et al. (2016) and Loison et al. (2017). In particular, dust-grain chemistry plays an important role in the formation of precursors to $CH_2CHCHCH_2$, i.e., the hydrogenation of three-carbon hydrocarbons (Hickson et al. 2016).

These three-carbon hydrocarbons hydrogenate so efficiently on grain surfaces that their gas-phase abundance is significantly affected by the desorption mechanism and related binding energies. The binding energies (E_b) of closed-shell molecules can be probed using temperature-programmed desorption (TPD) experiments. A value of $E_b = 2500$ K for CH_3CCH from itself (i.e., in the multilayer regime) was extracted from kinetic modeling of experiments involving reactions between O atoms and CH_3CCH (Kimber et al. 2014). Using the same method, CH_3CHCH_2 was found to have an E_b of similar magnitude (2580 K; Ward & Price 2011). Recently, Behmard et al. (2019) reported a mean $E_b = 4400$ K for CH_3CCH, 3800 K for CH_3CHCH_2, and 3500 K for $CH_3CH_2CH_3$ from amorphous solid water (ASW) ice. These values are significantly higher than those that have been computed for E_b on model water substrates, e.g., $E_b(CH_3CCH) = 2342$ K from water tetramers, $E_b(CH_3CCH) = 3153$ K from water hexamers, and $E_b(CH_3CH_2CH_3) = 1456$ K from water monomers (Das et al. 2018; Srivastav et al. 2022). We chose to use the values reported by Behmard et al. (2019) in our models since the authors derived the binding energies directly from TPD

analysis from ASW ice, which is likely representative of the ice surfaces present in TMC-1. We find that the higher binding energies measured by Behmard et al. (2019) decelerated the release of $CH_2CHCHCH_2$ and its precursors into the gas phase, compared to using the lower binding energies recommended from theoretical studies. In the case of radical species, we used the computed binding energies listed in Wakelam et al. (2017), which are 3100 K for both $CHCHCH_3$ and $CH_3CH_2CH_2$. As there is no information on the binding energies of $CH_2CHCHCH_2$, 1-C_4H_5CN, and c-C_5H_5N, we used the additive law to estimate those values (Cuppen & Herbst 2007), i.e., $E_b(\text{butadiene}) = E_b(C_2H_3) + E_b(C_2H_3) = 5600$ K.

4.2. Isomer-specific Chemistry

It is important to reiterate that our model does not distinguish between isomers of 1-C_4H_5CN. Morales et al. (2011) measured the overall rate coefficient for the reaction of CN + $CH_2CHCHCH_2$ by following the time-dependent signal from the CN radical via laser-induced fluorescence. While no information is obtained about the nature of the reaction products using this technique, the authors also conducted crossed molecular beam experiments and measured a branching ratio of ~99% to the 1-C_4H_5CN product channel; however, these experiments do not distinguish between the *E*- and *Z*-isomers. Because our observations only measure the abundance of the *E*-isomer, and our model represents the sum of the two isomers, care should be taken before direct comparisons are made. Further observational constraints on the *Z*-isomer and laboratory constraints on the branching ratio would be highly valuable.

As for butadiene, a source of uncertainty in its production and reactivity is the role of its minor conformational isomer *gauche*-butadiene, which lies about 2.9 kcal mol^{-1} higher in energy than the major *trans* conformer (Saltiel et al. 2001). Theoretical studies have focused almost exclusively on *trans*-butadiene, and most experimental studies have been unable to distinguish between the *trans* and *gauche* conformers. In TMC-1, the *trans*-to-*gauche* ratio is likely kinetically controlled because of the 3 kcal mol^{-1} barrier for the isomerization of *gauche* to *trans*, and therefore the *gauche* conformer might represent a nonnegligible portion of the total butadiene abundance. Although the total neutral–neutral reactivity of *gauche*-butadiene with radicals like C_2H and CH can reasonably be speculated to be similar to that of *trans*, the product branching ratios, particularly those to cyclic species, might differ considerably given that the *gauche* geometry is already close to a planar, cyclic carbon framework (Baraban et al. 2018).

The unknown kinetics of *gauche*-butadiene might also contribute to the discrepancies between the flow reactor (Lockyear et al. 2015) and crossed molecular beam (Jones et al. 2011) laboratory measurements of the $CH_2CHCHCH_2$ + C_2H reaction. The former experiments take place in thermal conditions at 298 K under which the *gauche* population is about 1%. The *gauche* population in the molecular beam experiments is unknown. Other work has shown that the butadiene conformational temperature can be highly out of equilibrium with the translational and rotational temperatures in a supersonic expansion (Baraban et al. 2018). Although the rest frequencies of *gauche*-butadiene are known, its small dipole moment (~0.1 D) makes its astronomical detection difficult. Based on the current DR4 data set, we can only place a conservative upper bound of 1.28×10^{11} cm^{-2}. As with *trans*-butadiene, the cyano derivative presents a likelier detection candidate. The rest frequencies of the *gauche* conformers of 1-C_4H_5CN are presently unknown. Follow-up laboratory measurements are thus necessary to enable a search in TMC-1. Understanding what role, if any, *gauche*-butadiene plays in the formation of cyclic species will also require new theoretical investigations and isomer-specific experimental reaction studies.

4.3. Pyridine

The detection of 1-C_4H_5CN, will be particularly significant due to its chemical relationship to c-C_5H_5N. c-C_5H_5N is an aromatic heterocyclic molecule of substantial astrochemical and astrobiological interest that has thus far eluded detection in the ISM (Batchelor et al. 1973; Charnley et al. 2005), including in our own search (Barnum et al. 2022). c-C_5H_5N is substantially less polar than 1-C_4H_5CN ($\mu = 2.2$ D and $\mu = 4.6$ D, respectively), which makes it more difficult to detect. The astrobiological relevance of c-C_5H_5N stems from its chemical similarity to pyrimidine (1,3-diazabenzene; c-$C_4H_4N_2$), which itself is a precursor to the DNA nucleobases cytosine, thymine, and uracil. In addition, key biomolecules nicotinic acid (vitamin B3) and nicotinamide are composed of functionalized c-C_5H_5N rings. Nicotinic acid has been detected in the Murchison meteorite (Pizzarello et al. 2004; Pizzarello & Huang 2005), which implies the possibility of its origin in interstellar space. A possible route to nicotinic acid from c-C_5H_5N in interstellar ices has been suggested (McMurtry et al. 2016).

It is currently unknown whether the cyano-butadienes are chemically linked to c-C_5H_5N as precursors or decomposition products. c-C_5H_5N is the lowest-energy isomer (B3LYP/6-311 +G(2d,p); Zdanovskaia et al. 2021), ~23.2 kcal mol^{-1} lower in energy than 1-C_4H_5CN, the lowest-energy acyclic isomer. 1-C_4H_5CN is itself 0.3 and 16.3 kcal mol^{-1} lower in energy than *Z*-1-cyano-1,3-butadiene and 4-cyano-1,2-butadiene, respectively. Identification of c-C_5H_5N in interstellar clouds would be valuable to our understanding of the chemical link between prebiotic molecules in interstellar clouds and those identified in meteorites, as well as our understanding of the formation of polycyclic aromatic nitrogen heterocycles (PANHs). The PANHs 1,4-dihydro(iso)quinoline and (iso) quinoline can be synthesized through reaction of pyridyl radicals with $CH_2CHCHCH_2$, and thus observational constraints of both of these precursors (or their proxies) are sought.

It remains unclear whether c-C_5H_5N can form in cold molecular clouds like TMC-1. The reaction of CN with $CH_2CHCHCH_2$ has been proposed; however, crossed molecular beam dynamic studies identified the 1-C_4H_5CN isomer as the dominant reaction product, with possible minor fractions of the aromatic c-C_5H_5N isomer. Other mechanisms that have been suggested include the ring expansion of pyrrole (C_4H_4NH) by CH (Soorkia et al. 2010), and the reaction of the cyanovinyl radical (C_3H_2N) with vinyl cyanide (CH_2CHCN; Parker et al. 2015). Additional experiments under low-temperature kinetic conditions would be valuable to elucidate whether the dominant product is anticipated to be the cyclic or acyclic isomer in TMC-1. In addition, branching ratios to the *E*- and *Z*-isomers would help to further constrain our models and inform future searches. Experimental setups are currently being developed, such as the chirped-pulse in uniform flow technique (Oldham et al. 2014; Abeysekera et al. 2015; Hays et al. 2020) and CRESU-SOL (Durif et al. 2021), that

may be able to shed further light on this reaction in the coming years.

5. Conclusions

We report the detection of s-*trans*-*E*-1-cyano-1,3-butadiene (1-C_4H_5CN), an acyclic isomer of pyridine (*c*-C_5H_5N), using the fourth data reduction of the GOTHAM deep spectral survey toward TMC-1 with the 100 m GBT. We performed velocity stacking and matched-filter analyses using MCMC simulations, and find evidence for the presence of this molecule at the 5.1σ level. We derive a total column density of $3.8^{+1.0}_{-0.9} \times 10^{10}$ cm^{-2}, which is predominantly found toward two velocity components. We use this molecule as a proxy for the apolar hydrocarbon 1,3-butadiene ($CH_2CHCHCH_2$), and using the three-phase astrochemical model `NAUTILUS` we determine a predicted peak column density for $CH_2CHCHCH_2$ of 2.34×10^{10}cm^{-2}. Using the 1-C_4H_5CN:$CH_2CHCHCH_2$ ratio derived in our model and the observed column density of 1-C_4H_5CN, we further constrain the total column density of 1,3-butadiene in TMC-1 to 3.94×10^{11} cm^{-2}. We discuss implications for bottom-up formation routes to aromatic and polycyclic aromatic molecules.

6. Data Access and Code

The data used for the MCMC analysis can be found in the DataVerse entry (GOTHAM Collaboration 2020). The code used to perform the analysis is part of the `molsim` open-source package; an archival version of the code can be accessed at Lee et al. (2021a).

I.R.C. acknowledges funding from the University of British Columbia, NSERC and the Canada Foundation for Innovation. C.X. thanks V. Wakelam for use of the `NAUTILUS` v1.1 code. B.A.M. and C.X. gratefully acknowledge the support of NSF grant No. AST-2205126. The National Radio Astronomy Observatory is a facility of the National Science Foundation operated under cooperative agreement by Associated Universities, Inc. The Green Bank Observatory is a facility of the National Science Foundation operated under cooperative agreement by Associated Universities, Inc.

Facility: GBT.

Software: `NAUTILUS` v1.1 (Ruaud et al. 2016), `Molsim` (Lee et al. 2021a), `Emcee` (Foreman-Mackey et al. 2013), `ArViz` (Kumar et al. 2019).

Appendix A
Markov Chain Monte Carlo Analysis Results

The corner plots resulting from the analysis of cyanobutadiene are shown in Figures A1 and A2, respectively. The velocity-stacked and matched-filter spectra using the posteriors derived from the two-component model are shown in Figure A3.

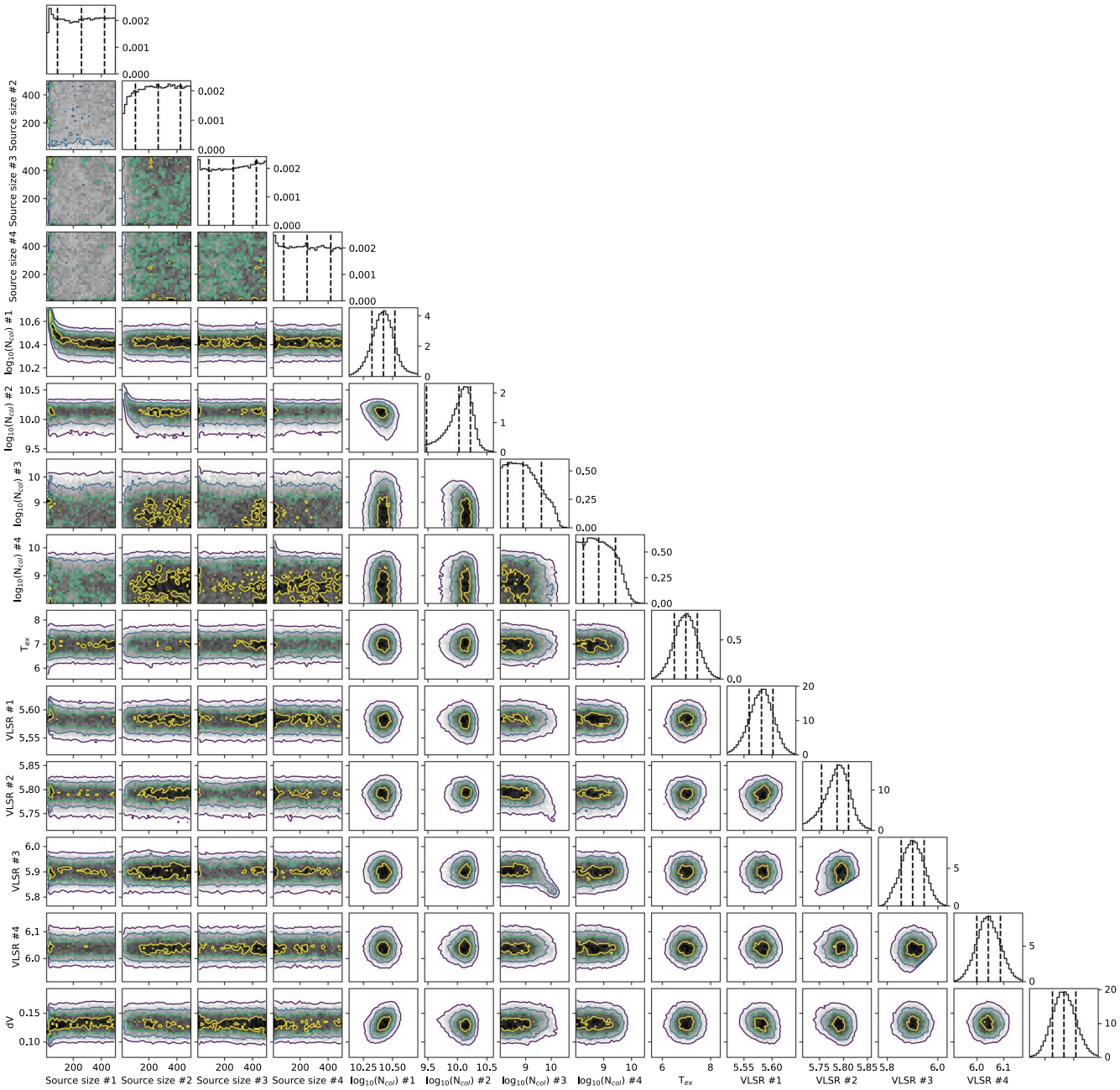

Figure A1. Corner plot for cyano-butadiene showing parameter covariances and marginalized posterior distributions for the MCMC fit; 16th, 50th, and 84th confidence intervals (corresponding to $\pm 1\sigma$ for a Gaussian posterior distribution) are shown as vertical lines.

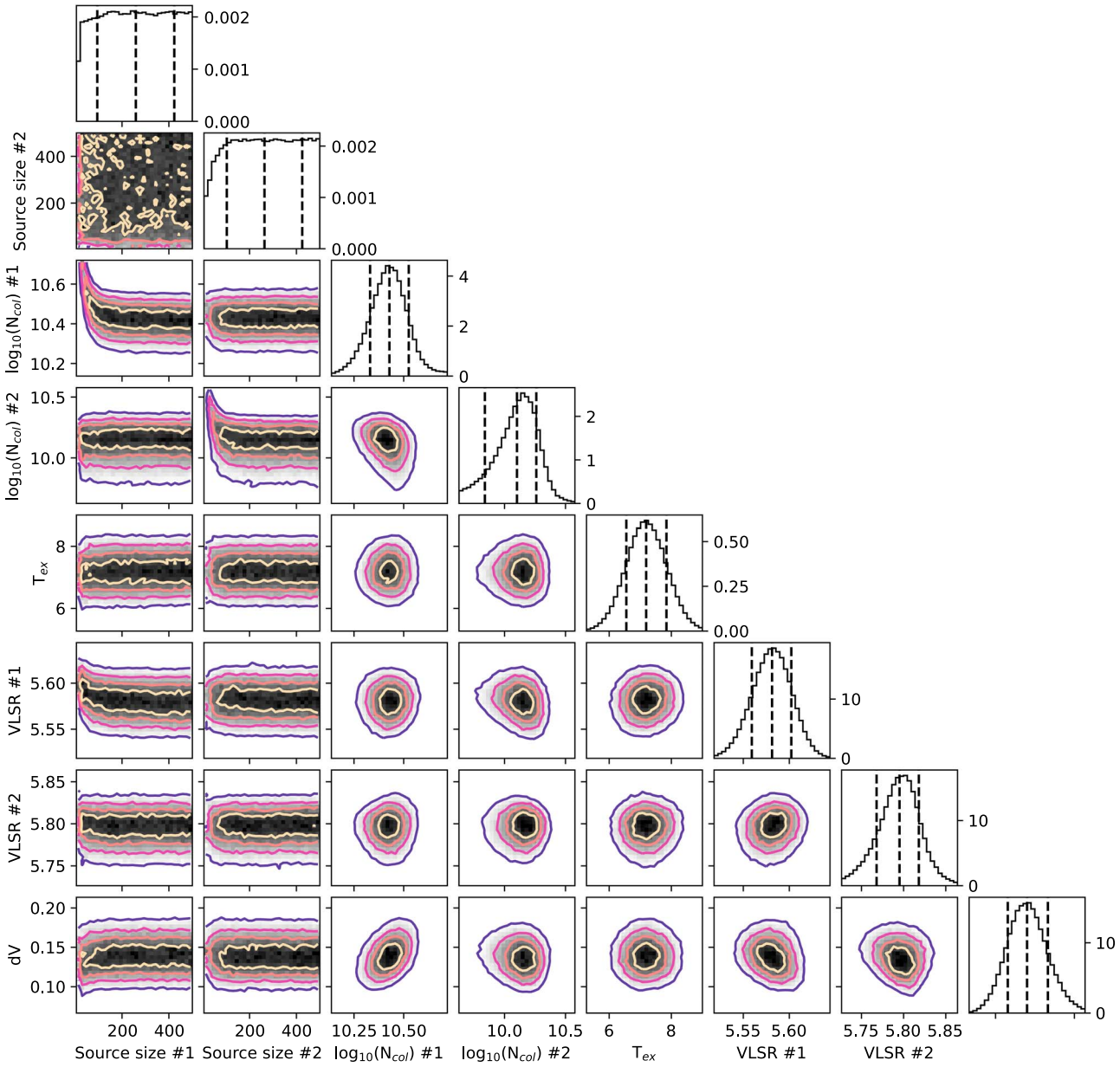

Figure A2. Corner plot for cyano-butadiene showing parameter covariances and marginalized posterior distributions for the MCMC fit; 16th, 50th, and 84th confidence intervals (corresponding to $\pm 1\sigma$ for a Gaussian posterior distribution) are shown as vertical lines.

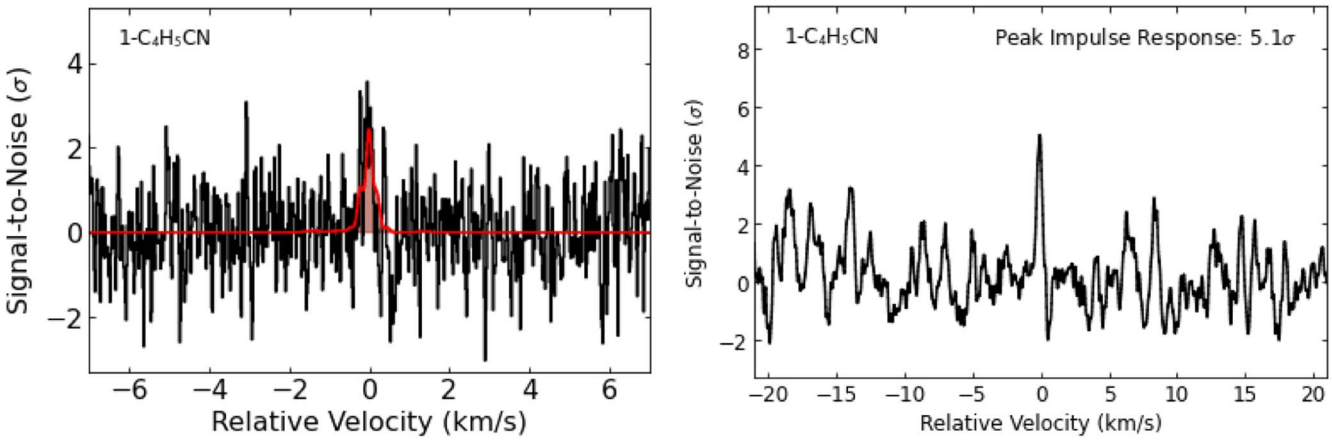

Figure A3. Velocity-stacked and matched-filter spectra of CN-butadiene, using the two-component MCMC analysis. The intensity scales are the S/Ns of the response functions when centered at a given velocity. The "zero" velocity corresponds to the channel with the highest intensity to account for blended spectroscopic transitions and variations in velocity component source sizes. Left: the stacked spectra from the GOTHAM DR4 data are displayed in black, overlaid with the expected line profile in red from our MCMC fit to the data. The S/N is on a per-channel basis. Right: matched-filter response obtained from cross-correlating the simulated and observed velocity stacks in the left panel; value annotated corresponds to the peak impulse response of the matched filter.

A.1. Spectroscopic Catalogs

In our initial search for individual lines of the cyano-butadiene isomers, we detected faint transitions at ∼19415.4 MHz (Figure A4), which are within ∼5 kHz of the $J_{K_a,K_c} = 7_{1,7}$ –$6_{1,6}$ hyperfine transitions of *E*-1-cyano-1,3-butadiene based on the predicted frequencies from laboratory measurements (McCarthy et al. 2020; Zdanovskaia et al. 2021). These predictions have an estimated uncertainty of less than 1 kHz, suggesting the astronomical features are interlopers, but because the $7_{1,7}$–$6_{1,6}$ transition was not directly observed in the original laboratory studies this assignment is uncertain.

To resolve this ambiguity, we performed new measurements of these and several other rotational transitions of *E*-1-cyano-1,3-butadiene using the same cavity Fourier-transform microwave spectrometer, discharge expansion source, and conditions as the initial laboratory study (McCarthy et al. 2020), except for switching to a more efficient precursor mix of 1,3-butadiene and acrylonitrile instead of benzene and nitrogen. All three ^{14}N quadrupole hyperfine components for the previously unreported $7_{1,7}$–$6_{1,6}$, $7_{0,7}$–$6_{0,6}$, $7_{1,6}$–$6_{1,5}$, and $5_{1,5}$–$4_{1,4}$ rotational transitions were observed. Their rest frequencies are in uniform agreement with the catalog predictions to within the measurement uncertainty (2 kHz). We conclude that the features observed astronomically are indeed interlopers and thus removed the overlapping cyano-butadiene transition from the analysis.

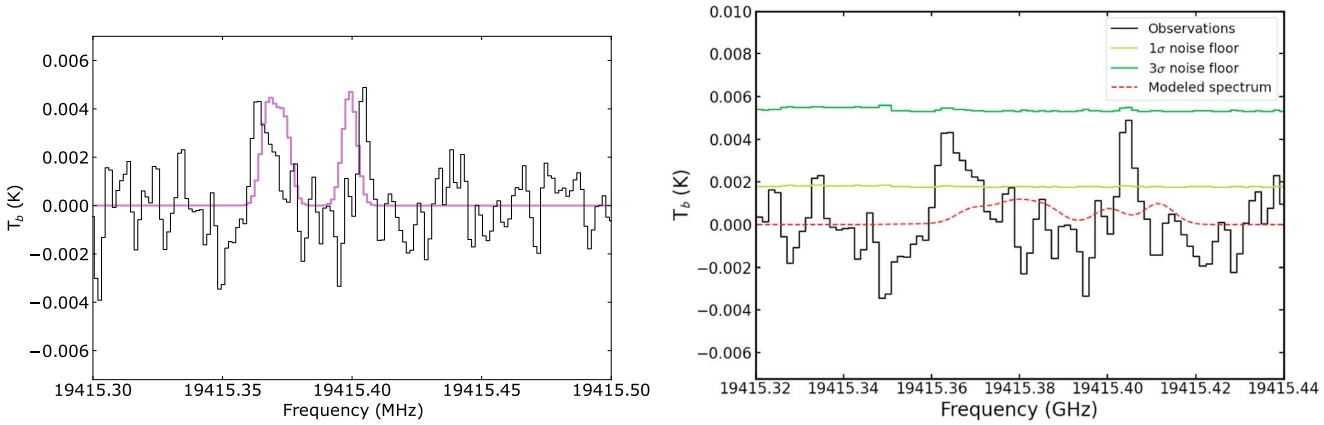

Figure A4. Left: weak interlopers detected in DR4 (black) at ∼19415.4 MHz and a simulated single-velocity component spectrum (purple) showing the $J = 7_{1,7} \rightarrow 6_{1,6}$ hyperfine transitions reported in Zdanovskaia et al. (2021). Right: simulated spectrum (red dashed line) using the outputs of the four-component MCMC analysis. The green and yellow lines indicate the 1σ and 3σ noise floors, respectively.

Appendix B
Reaction Network and Uncertainties

The proposed production and destruction routes involving 1-C_4H_5CN and c-C_5H_5N are listed in Table B1. Definitions of α, β, and γ can be found on the KIDA online database (http://kida.astrophy.u-bordeaux.fr/help.html). The formulae of type 3 and 4 are $k(T) = \alpha(T/300)^{\beta}e^{-\gamma/T}$ and $k(T) = \alpha\beta(0.62 + 0.4767\gamma(300/T)^{0.5})$, where k is in cubic centimeters per second and T is in kelvins, respectively. The corresponding rate coefficients at 10 K are also listed.

We report the modeled abundances to three digits. The accuracy of the modeled values may be lower with the consideration of uncertainties in the input parameters such as initial conditions and rate coefficients. However, it is infeasible to estimate the accuracy of the modeled values because of, for example, the difficulty in determining the order of accuracy of the nontrivial numerical methods used to solve the rate equations. As such, the presented values were obtained in a realization of the numerical model using the exact values of the input parameters described above. The modeled values in this case are accurate to up to 16 digits, minus the accuracy of the numerical method, which presumably gives results far more accurate than three digits. We present only three digits in order to match the precision of the observed values.

Table B1
Summary of the Proposed Reactions for c-C_5H_5N and 1-C_4H_5CN

Reactions	α	β	γ	Formula Type	k(10K)	Reference
Production Routes:						
$CN + CH_2CHCHCH_2 \longrightarrow H + 1\text{-}C_4H_5CN$	4.752×10^{-10}	0	9.266	3	1.881×10^{-10}	(Morales et al. 2011; Parker et al. 2015)
$CN + CH_2CHCHCH_2 \longrightarrow H + c\text{-}C_5H_5N$	4.800×10^{-12}	0	9.266	3	1.900×10^{-12}	(Morales et al. 2011; Parker et al. 2015)
Destruction Routes:						
$HCO+ + 1\text{-}C_4H_5CN \longrightarrow CO + CH_3CHCH_2 + C_2N+$	1.0	1.694×10^{-9}	5.003	4	2.318×10^{-8}	Capture-rate theory
$H_3O+ + 1\text{-}C_4H_5CN \longrightarrow H_2O + CH_3CHCH_2 + C_2N^+$	1.0	1.994×10^{-9}	5.003	4	2.728×10^{-8}	Capture-rate theory
$H_3^+ + 1\text{-}C_4H_5CN \longrightarrow H_2 + CH_3CHCH_2 + C_2N^+$	1.0	4.589×10^{-9}	5.003	4	6.279×10^{-8}	Capture-rate theory
$He^+ + 1\text{-}C_4H_5CN \longrightarrow He + C_4H_5^+ + CN$	1.0	3.998×10^{-9}	5.003	4	5.470×10^{-8}	Capture-rate theory
$H^+ + 1\text{-}C_4H_5CN \longrightarrow H + C_4H_5^+ + CN$	0.50	7.851×10^{-9}	5.003	4	5.371×10^{-8}	Capture-rate theory
$H^+ + 1\text{-}C_4H_5CN \longrightarrow H_2 + C_5H_4N^+$	0.50	7.851×10^{-9}	5.003	4	5.371×10^{-8}	Capture-rate theory
$C^+ + 1\text{-}C_4H_5CN \longrightarrow C + C_4H_5^+ + CN$	0.33	2.417×10^{-9}	5.003	4	1.102×10^{-8}	Capture-rate theory
$C^+ + 1\text{-}C_4H_5CN \longrightarrow CN + C_5H_5^+$	0.33	2.417×10^{-9}	5.003	4	1.102×10^{-8}	Capture-rate theory
$C^+ + 1\text{-}C_4H_5CN \longrightarrow C_2N^+ + CH_2CHC_2H+ H$	0.33	2.417×10^{-9}	5.003	4	1.102×10^{-8}	Capture-rate theory
$HCO^+ + c\text{-}C_5H_5N \longrightarrow CO + CH_3CHCH_2 + C_2N^+$	1.0	1.561×10^{-9}	2.470	4	1.103×10^{-8}	Capture-rate theory
$H_3^+ + c\text{-}C_5H_5N \longrightarrow H_2 + CH_3CHCH_2 + C_2N^+$	1.0	4.229×10^{-9}	2.470	4	2.990×10^{-8}	Capture-rate theory
$H_3O^+ + c\text{-}C_5H_5N \longrightarrow H_2O + CH_3CHCH_2 + C_2N^+$	1.0	1.837×10^{-9}	2.470	4	1.299×10^{-8}	Capture-rate theory
$He^+ + c\text{-}C_5H_5N \longrightarrow He + C_4H_5^+ + CN$	1.0	3.685×10^{-9}	2.470	4	2.605×10^{-8}	Capture-rate theory
$H^+ + c\text{-}C_5H_5N \longrightarrow H + C_4H_5^+ + CN$	0.33	7.235×10^{-9}	2.470	4	1.705×10^{-8}	Capture-rate theory
$H^+ + c\text{-}C_5H_5N \longrightarrow H_2 + C_5H_4N+$	0.33	7.235×10^{-9}	2.470	4	1.705×10^{-8}	Capture-rate theory
$H^+ + c\text{-}C_5H_5N \longrightarrow CH_3CHCH_2 + C_2N^+$	0.33	7.235×10^{-9}	2.470	4	1.705×10^{-8}	Capture-rate theory
$C^+ + c\text{-}C_5H_5N \longrightarrow C + C_4H_5^+ CN$	1.0	2.228×10^{-9}	2.470	4	1.575×10^{-8}	Capture-rate theory

ORCID iDs

Ilsa R. Cooke https://orcid.org/0000-0002-0850-7426
Ci Xue https://orcid.org/0000-0003-2760-2119
P. Bryan Changala https://orcid.org/0000-0003-0304-9814
Alex N. Byrne https://orcid.org/0000-0002-4593-518X
Kin Long Kelvin Lee https://orcid.org/0000-0002-1903-9242
Ryan A. Loomis https://orcid.org/0000-0002-8932-1219
Thanja Lamberts https://orcid.org/0000-0001-6705-2022
Anthony Remijan https://orcid.org/0000-0001-9479-9287
Andrew M. Burkhardt https://orcid.org/0000-0003-0799-0927
Eric Herbst https://orcid.org/0000-0002-4649-2536
Michael C. McCarthy https://orcid.org/0000-0001-9142-0008
Brett A. McGuire https://orcid.org/0000-0003-1254-4817

References

Abeysekera, C., Joalland, B., Ariyasingha, N., et al. 2015, JPhCh Lett., 6, 1599
Balucani, N., Asvany, O., Huang, L. C. L., et al. 2000, ApJ, 545, 892
Baraban, J. H., Martin-Drumel, M.-A., Changala, P. B., et al. 2018, AngCh, 57, 1821
Barnum, T. J., Siebert, M. A., Lee, K. L. K., et al. 2022, JPCA, 126, 2716
Batchelor, R. A., Brooks, J. W., Godfrey, P. D., & Brown, R. D. 1973, AuJPh, 26, 557
Behmard, A., Fayolle, E. C., Graninger, D. M., et al. 2019, ApJ, 875, 73
Burkhardt, A. M., Loomis, R. A., Shingledecker, C. N., et al. 2021a, NatAs, 5, 181
Burkhardt, A. M., Long Kelvin Lee, K., Bryan Changala, P., et al. 2021b, ApJL, 913, L18
Cernicharo, J., Agúndez, M., Cabezas, C., et al. 2021a, A&A, 649, L15
Cernicharo, J., Agúndez, M., Kaiser, R. I., et al. 2021b, A&A, 652, L9
Cernicharo, J., Agúndez, M., Kaiser, R. I., et al. 2021c, A&A, 655, L1
Cernicharo, J., Fuentetaja, R., Agúndez, M., et al. 2022, A&A, 663, L9
Charnley, S. B., Kuan, Y.-J., Huang, H.-C., et al. 2005, AdSpR, 36, 137
Chin, C.-H., Chen, W.-K., Huang, W.-J., Lin, Y.-C., & Lee, S.-H. 2013, Icar, 222, 254
Cooke, I. R., Gupta, D., Messinger, J. P., & Sims, I. R. 2020, ApJL, 891, L41
Cuppen, H. M., & Herbst, E. 2007, ApJ, 668, 294
Das, A., Sil, M., Gorai, P., Chakrabarti, S. K., & Loison, J. C. 2018, ApJS, 237, 9
Daugey, N., Caubet, P., Retail, B., et al. 2005, PCCP, 7, 2921
Dobashi, K., Shimoikura, T., Nakamura, F., et al. 2018, ApJ, 864, 82
Dobashi, K., Shimoikura, T., Ochiai, T., et al. 2019, ApJ, 879, 88
Durif, O., Capron, M., Messinger, J. P., et al. 2021, RSciI, 92, 014102
Foreman-Mackey, D., Hogg, D. W., Lang, D., & Goodman, J. 2013, PASP, 125, 306
GOTHAM Collaboration 2020, Spectral Stacking Data for Phase 2 Science Release of GOTHAM, V3, doi:10.7910/DVN/K9HRCK
Gratier, P., Majumdar, L., Ohishi, M., et al. 2016, ApJS, 225, 25
Gray, C., Gubbins, K., & Joslin, C. 1984, Theory of Molecular Fluids: I: Fundamentals, International Series of Monographs on Chemistry (Oxford: Oxford Univ. Press), https://books.google.com/books?id=3mz2RcnnMGwC
Hays, B. M., Guillaume, T., Hearne, T. S., et al. 2020, JQSRT, 250, 107001
Hickson, K. M., Wakelam, V., & Loison, J.-C. 2016, MolAs, 3, 1
Hincelin, U., Wakelam, V., Hersant, F., et al. 2011, A&A, 530, A61
Jones, B. M., Zhang, F., Kaiser, R. I., et al. 2011, PNAS, 108, 452
Kaiser, R. I., Stranges, D., Lee, Y. T., & Suits, A. G. 1997, ApJ, 477, 982
Kimber, H. J., Ennis, C. P., & Price, S. D. 2014, FaDi, 168, 167
Kougias, S. M., Knezz, S. N., Owen, A. N., et al. 2020, JOrCh, 85, 5787
Kumar, R., Carroll, C., Hartikainen, A., & Martin, O. 2019, JOSS, 4, 1143
Lee, K. L. K., Loomis, R. A., & McGuire, B. A. 2021a, molsim v0.3.0, Zenodo, doi:10.5281/zenodo.4560750
Lee, K. L. K., Changala, P. B., Loomis, R. A., et al. 2021b, ApJL, 910, L2
Lee, K. L. K., & McCarthy, M. 2019, JPhCh Lett., 10, 2408
Lockyear, J. F., Fournier, M., Sims, I. R., et al. 2015, IJMSp, 378, 232
Loison, J.-C., Agúndez, M., Wakelam, V., et al. 2017, MNRAS, 470, 4075
Loison, J.-C., & Bergeat, A. 2009, PCCP, 11, 655
Loomis, R. A., Burkhardt, A. M., Shingledecker, C. N., et al. 2021, NatAs, 5, 2
McCarthy, M. C., Lee, K. L. K., Carroll, P. B., et al. 2020, JPCA, 124, 5170
McCarthy, M. C., Lee, K. L. K., Loomis, R. A., et al. 2021, NatAs, 5, 176
McGuire, B. A., Burkhardt, A. M., Kalenskii, S. V., et al. 2018, Sci, 359, 202
McGuire, B. A., Burkhardt, A. M., Loomis, R. A., et al. 2020, ApJL, 900, L10
McGuire, B. A., Loomis, R. A., Burkhardt, A. M., et al. 2021, Sci, 371, 1265
McMurtry, B. M., Turner, A. M., Saito, S. E., & Kaiser, R. I. 2016, CP, 472, 173
Morales, S. B., Bennett, C. J., Le Picard, S. D., et al. 2011, ApJ, 742, 26
Nelson, R., Lide, D., & Maryott, A. 1967, Selected Values of Electric Dipole Moments for Molecules in the Gas Phase NSRDS-NBS (Gaithersburg, MD: U.S. National Bureau of Standards), doi:10.6028/NBS.NSRDS.10
Oldham, J. M., Abeysekera, C., Joalland, B., et al. 2014, JChPh, 141, 154202
Parker, D. S. N., Kaiser, R. I., Kostko, O., et al. 2015, ApJ, 803, 53
Parker, D. S. N., Kaiser, R. I., Kostko, O., et al. 2015, PCCP, 17, 32000
Pizzarello, S., & Huang, Y. 2005, GeCoA, 69, 599
Pizzarello, S., Huang, Y., & Fuller, M. 2004, GeCoA, 68, 4963
Ruaud, M., Wakelam, V., & Hersant, F. 2016, MNRAS, 459, 3756
Saltiel, J., Sears, D. F., & Turek, A. M. 2001, JPCA, 105, 7569
Shingledecker, C. N., Lee, K. L. K. , Wandishin, J. T., et al. 2021, A&A, 652, L12
Sims, I. R., Queffelec, J.-L., Travers, D., et al. 1993, CPL, 211, 461
Sita, M. L., Changala, P. B., Xue, C., et al. 2022, ApJL, 938, L12
Smith, S. E. T., Friesen, R., Marchal, A., et al. 2023, MNRAS, 519, 285
Soorkia, S., Taatjes, C. A., Osborn, D. L., et al. 2010, PCCP, 12, 8750
Srivastav, S., Sil, M., Gorai, P., et al. 2022, MNRAS, 515, 3524
Sun, B. J., Huang, C. H., Chen, S. Y., et al. 2014, JPCA, 118, 7715
Trevitt, A. J., Prendergast, M. B., Goulay, F., et al. 2013, JPCA, 117, 6450
Turner, B. E. 1991, ApJS, 76, 617
Wakelam, V., Loison, J. C., Herbst, E., et al. 2015, ApJS, 217, 20
Wakelam, V., Loison, J. C., Mereau, R., & Ruaud, M. 2017, MolAs, 6, 22
Ward, M. D., & Price, S. D. 2011, ApJ, 741, 121
Woon, D. E., & Herbst, E. 2009, ApJS, 185, 273
Xue, C., Willis, E. R., Loomis, R. A., et al. 2020, ApJ, 900, L9
Zdanovskaia, M. A., Dorman, P. M., Orr, V. L., et al. 2021, JAChS, 143, 9551